Wind Energy

WILEY

RESEARCH ARTICLE OPEN ACCESS

Segmented Gurney Flaps for Improved Wind Turbine Wake Recovery

Nirav Dangi[1,2] | Koen Boorsma[1] | Edwin Bot[1] | Wim Bierbooms[2] | Wei Yu[2]

[1]Wind Energy, Netherlands Organisation for Applied Scientific Research (TNO), Petten, Netherlands | [2]Aerospace Engineering, Delft University of Technology (TU Delft), Delft, Netherlands

Correspondence: Koen Boorsma (koen.boorsma@tno.nl)

Received: 23 October 2024 | **Revised:** 9 November 2025 | **Accepted:** 23 December 2025

Keywords: field tests | Gurney flap | LiDAR | wake

ABSTRACT

When wind passes through the rotor of a wind turbine, the velocity is decreased while turbulence is increased. The region of decreased wind speed behind the rotor is known as the wind turbine wake and is bounded by a complex structure of helical vortices. This structure occurs to be more stable in low ambient turbulence and low tip speed ratio conditions, leading to a delayed recovery of the wake. The diminished wind speed in the wake leads to a decline in power output for downstream wind turbines, with this loss scaling proportionally to the cube of the velocity. This study uses field tests and simulations to evaluate enhanced wake recovery with segmented Gurney flaps on a 3.8-MW research wind turbine. Four Gurney flaps were attached at regions near the tip of each blade. This configuration is hypothesized to induce turbulence that destabilizes the vortex system, resulting in faster wake recovery. Field tests using a scanning LiDAR were conducted to quantify the wind turbine wake recovery between the baseline and the retrofitted configuration in various atmospheric conditions. The results show a consistent increase in wake recovery for the Gurney flap configuration, generally at all downstream distances. This was illustrated by a reduction of axial velocity deficits of roughly 10% at hub height, at five diameters downstream distance. The influence of retrofitting on turbine power and loads was limited. Summarizing, a very successful field test campaign was executed, which demonstrated the use of segmented Gurney flaps as a promising add-on to promote enhanced wind turbine wake recovery for improved overall wind farm performance.

1 | Introduction

The wind turbine wake is a region of three-dimensional turbulent flow characterized by a velocity deficit and a complex structure of helical vortices. The wake of a single rotor blade consists of a continuous sheet of trailed vorticity due to the gradient of bound circulation along the blade span. It can be divided into three regions: the near wake, intermediate wake, and far wake [1, 2]. The near wake is defined as the region just behind the rotor where the presence of the wind turbine rotor is apparent by the number of blades and blade aerodynamics. The latter includes effects of stalled flow, 3-D effects, and the tip and root-vortex helices. In the far wake, the structure of helical vortices disappears and is transformed into a region of high diffusive vorticity, predominantly facilitating turbulence mixing. Concurrently, the wake experiences a revitalization process. Between these two regions, a third zone can be distinguished, the intermediate wake [2]. This region is a transition between the near wake and the far wake, starting with instabilities in the structure of helical vortices and ending with the breakdown of this system.

It is worth noting that the instability and breakdown of the helical system of vortices in the transition region affects the development of the turbulence in the far wake, where the mixing process between the inner and the outer flow regions occurs. Moreover, in low ambient turbulence and low tip speed ratio

conditions, the structure of helical vortices is much more stable. This results in reduced turbulent mixing, leading to elevated velocity deficits within the wake. The velocity deficits in wind turbine wakes are critical for bigger wind farms, where multiple turbines are grouped together and their different wake effects are combined. For a wind farm of 140 turbines with a spacing of five rotor diameters, the total energy loss due to wake effects can be more than 20% [3].

Researchers have proposed and investigated various wake control methods aimed at reducing the power loss for downstream wind turbines. These methods involve either redirecting the wind turbine wake away from subsequent turbines (wake steering) or diminishing the intensity of upstream wakes. This is usually achieved by enhancing wake mixing or adjusting the pitch to lower angles of attack, thereby altering the thrust coefficient.

Static axial induction control by pitch [4–6] or torque control [7, 8] and dynamic axial induction control [9, 10] by dynamic pitch control [11–13] usually fall into the latter category. Add-on devices focusing on faster wake mixing by use of actuating flaps [14–16], turbulators [17, 18], and winglets [18, 19] on the wind turbine blade tip are also evaluated in existing research. Gurney flaps have been evaluated mainly for load control of wind turbines in some studies, for example, in [20–22]. Similar to Gurney flaps, microtabs have been evaluated for load control, for example, in the research of [23–25]. However, most of the studies focus on root Gurney flaps, which operate in a different angle of attack regime than the tip Gurney flaps used in this study.

The Gurney flap, named after the race car driver Dan Gurney, is a simple, small tab (height usually lower than 2% of the airfoil chord) added to the trailing edge (perpendicular to the free-stream) of the pressure side of an airfoil. A Gurney flap can increase the lift considerably with only a small drag penalty. It also changes the downstream wake development [26], depending on the height of the Gurney flap. In [27], it was found that applying Gurney flaps results in the formation of counter-rotating vortices that exist up to long distances downstream. This can delay or eliminate the flow separation near the trailing edge on the upper surface, increasing the total suction, leading to an increased circulation with an enhanced lift. The Gurney flap provides a substantial increase in lift before the stall angle, after which the drag penalty causes a reduction in lift-to-drag ratio. Gurney flaps can extend across the entire span of a wing or be segmented, that is, positioned along specific spanwise sections. These are also known as miniature trailing edge effectors (MiTEs) [28, 29].

The wake of Gurney flaps has been investigated in the context of aircraft wings [29–33], but limited research is available for the application of Gurney flaps on wind turbine blades. In particular, segmented Gurney flaps for wake recovery have been evaluated on aircraft wings in the study of [29]. One of the configurations in their work shows similarities to the segmented Gurney flap configuration used in this study on wind turbine blades, consisting of four flaps along each blade tip. The expectations of wake recovery by the use of segmented Gurney flaps were clarified in their wind tunnel study. An intensification of tangential and stream-wise velocity components from the segmented Gurney flaps was observed. The increase in circulation due to the change in the span-wise loading was found to cause the intensification. The authors state that despite a smooth increment in the loading distribution in the configuration they experimented, a very small counter-rotating vortex pair also occurred at the flap tips, which was then advected by the strong mean flow due to the primary trailing vortex. The velocity deficit around the Gurney flap was noted to be associated with the increased drag; however, further downstream, it was no longer present; because as the vortex continued to roll up, the patches diffused into one another by being constantly advected by the strong tangential velocities (also seen in other studies [33, 34]). The effects of the segmented Gurney flaps were being felt by the vortex more and more as it continued to roll up.

From the experiments, the authors established that in order to significantly perturb the vortex, only 13% of the span needed to be deployed with Gurney flaps. The flaps were applied only near the tip of the wing, where the loading distribution varied the most. The insights on the intermediate wake from this study also confirmed that the effect of the segmented Gurney flaps upon the vortex was a lasting and reliable change. They also conclude that MiTEs (or segmented Gurney flaps) can be used to introduce spatial disturbances to a trailing vortex in both the span-wise and lift directions. Finally, they suggest that the use of MiTE configurations, which, if varied in time, may be useful for wake alleviation. This study on an aircraft wing provides a detailed relevant literature for the use of segmented Gurney flaps for wake mitigation.

The hypothesized working principle behind the use of segmented Gurney flaps is to alter the lift distribution along the blade span (at the tip). By achieving a jagged lift (Figure 1) and circulation distribution, additional vortices are shed from the edges of the Gurney flaps to perturb the stable tip vortex. This use of segmented Gurney flaps is hypothesized to destabilize

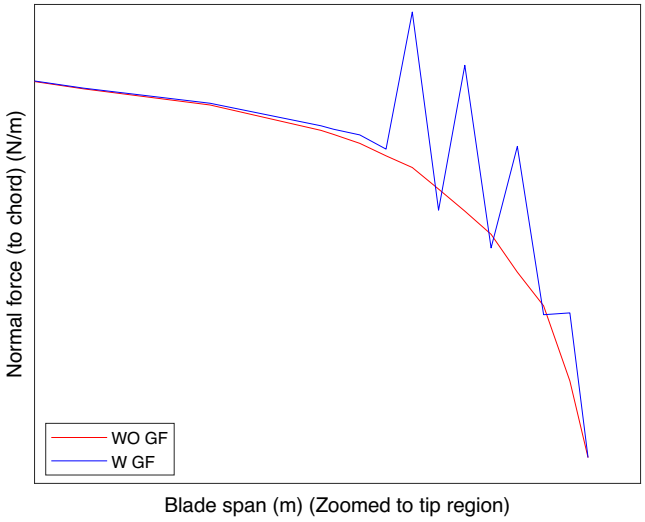

FIGURE 1 | Normal force distribution without and with segmented Gurney flaps on the 3.8-MW wind turbine blade (zoomed to the tip region).

the system of helical vortices. Additionally, a higher pressure drag from the Gurney flap is hypothesized to increase turbulence in the wake, which could contribute to the faster wake mixing.

Some gaps in the above mentioned literature on wake control techniques are the lack of full scale field wind turbine tests for further validation, evaluation of the effect of loading on the wind turbine on which the strategies are utilized, applicability at higher turbulence intensity levels, and practical concerns about the suspension of the devices on existing wind turbine blades. To overcome these gaps, this study evaluates segmented Gurney flaps for wind turbine blades with the following approach:

1. Setting up and conducting scanning LiDAR measurements in the wake (up to a distance of 5.5 times the rotor diameter downstream) for a 3.8-MW research wind turbine with and without segmented Gurney flaps.
2. Analyzing wake recovery (time averaged profiles) of both turbine configurations for different free stream wind speed, turbulence intensity, and wind direction conditions.
3. Analyzing power and loads of both turbine configurations using 10-min averaged measurement data.
4. Performing simulations to further assess the power and loads of the retrofitted wind turbine.

The next chapter details the methodology employed in this study. Following that, the setup of the field tests is explained in Sections 3 and 4. The results of the wake analysis are discussed in Section 5, and the results of the power and loads analysis are discussed in Section 6. Finally, concluding remarks and recommendations are placed in Section 7. Validation and background information on certain parameters are provided in the appendices.

2 | Methodology

The wind turbine under study was a 3.8-MW research wind turbine (RWT) with a rotor diameter of 130 m and a hub height of 110 m. The wind turbine is located at an onshore wind farm in the Netherlands, shown in Figure 2a. An aerial view of the test site is shown in Figure 2b, highlighting the locations of the RWT and the key measurement devices used in this study.

The RWT was retrofitted by adding four Gurney flaps to the tip region of each blade. The Gurney flaps were designed as a wedge with a length of 0.6 m and a height equal to 2 % of the local blade chord. The same height and width ensured a 45° wedge. In line with the literature, these dimensions were chosen to ensure a better lift-to-drag ratio than the typical rectangular Gurney flap [35, 36]. Figure 3a illustrates the dimensions.

In Figure 3b, the Gurney flaps installed on the wind turbine blade are identified. They were positioned with a gap of 0.6 m between each flap, covering approximately the last 7% of the blade span. This configuration is referred to as segmented Gurney flaps.

The Gurney flaps were manufactured from SikaBlock M940, resulting in a maximum weight of 130 g for one Gurney flap. The flaps were mounted on the wind turbine blades by technicians on a cherry picker, using Plexus MA 320 adhesive.

The field tests include a wind turbine wake analysis using a scanning LiDAR, as well as a power and loads analysis based on 10-min averaged measurements. Testing for the baseline configuration was carried out from September 01, 2022, to January 23, 2023, followed by testing of the retrofitted configuration from January 24 to February 14, 2023. To support and enhance the power and loads analysis, numerical simulations were also performed.

For the wake analysis, a Leosphere Vaisala Windcube 200S pulsed scanning LiDAR was used. To assess the inflow

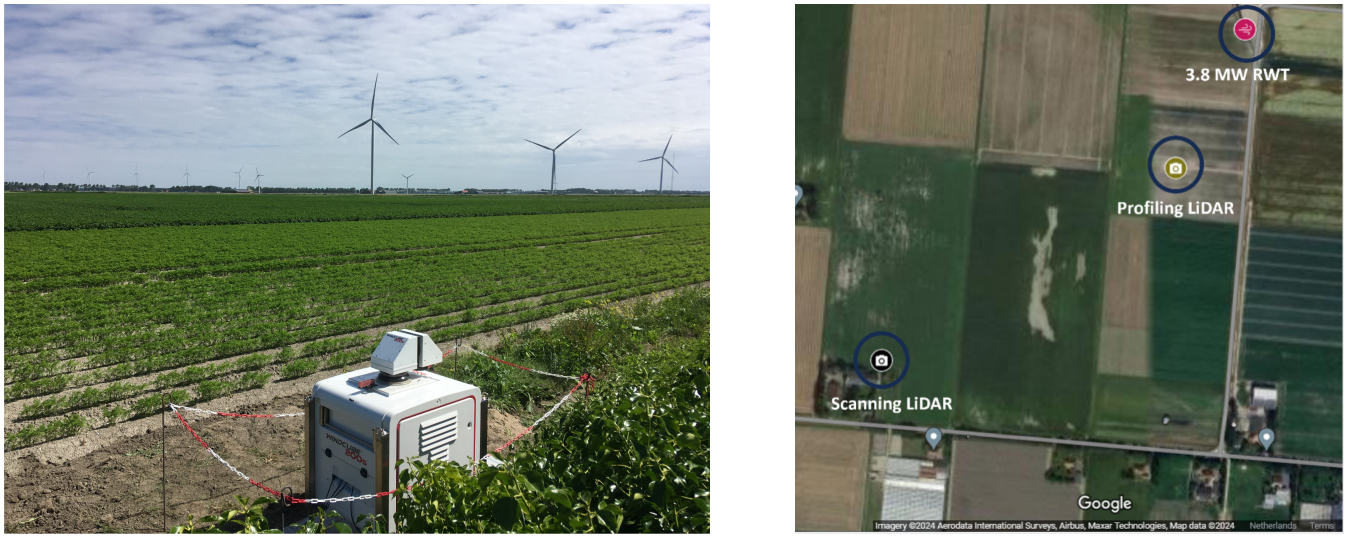

(a) Scanning LiDAR in the foreground.

(b) Aerial photo of the test site.

FIGURE 2 | Test site in Wieringermeer, the Netherlands (Photographed by TNO).

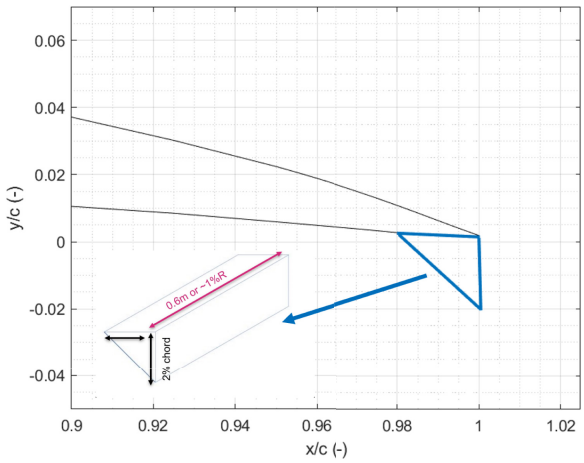

(a) Gurney flap designed as a wedge

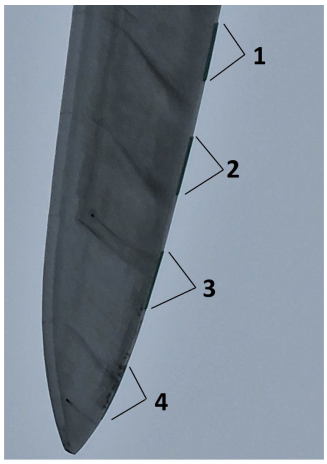

(b) Installed Gurney flaps (Photographed by TNO)

FIGURE 3 | Design and installation of the segmented Gurney flaps.

conditions, a ground-based profiling LiDAR was used, which was placed approximately 2.2D upstream. This ground-based profiling LiDAR was used to assess the inflow conditions at 11 different altitudes between 42 and 188 m.

The power and loads analysis of the field tests utilized measurement data averaged over 10-min intervals. The turbine was instrumented with strain gauges at the blade roots and tower base, which were calibrated to measure blade root and tower base moments.

To estimate the power and loads using simulations, dynamic blade element momentum theory (DBEM) was used from NREL OpenFAST [37], using an aero-elastic turbine description as specified by the manufacturer. The aero-elastic set-up was validated against measurements, and a non-confidential version of it is reported in [38]. The generation of airfoil polars for the Gurney flap configuration, as shown in Figure 3a, was performed using a steady inflow 2D computational fluid dynamics (CFD) study with Reynolds-averaged Navier-Stokes (RANS) modeling featuring the OpenFOAM software [39]. The $k-\omega$ SST turbulence model was used with a Y-plus value of 0.1, featuring an O-grid resulting in a mesh with 126750 grid cells. The boundary layer was modeled to be turbulent. Before generating the polars for airfoils with Gurney flaps, the CFD setup underwent validation by comparing simulation results of the airfoil polars without Gurney flaps to corresponding wind tunnel data available for steady inflow and tripped conditions. Due to the lack of experimental polar data for the Gurney flap-equipped airfoil, the generated polars were compared to those of other airfoils for which data were available in literature [34], in terms of the lift-curve slope, post-stall performance.

3 | Set Up and Data Processing of Wake Measurements

The undisturbed wind sector for the wind turbine under study was 180° to 340°, measured with respect to the North. This is shown in Figure 4, where the undisturbed sector is shown in blue, and the prevailing wind sector is shown in brown.

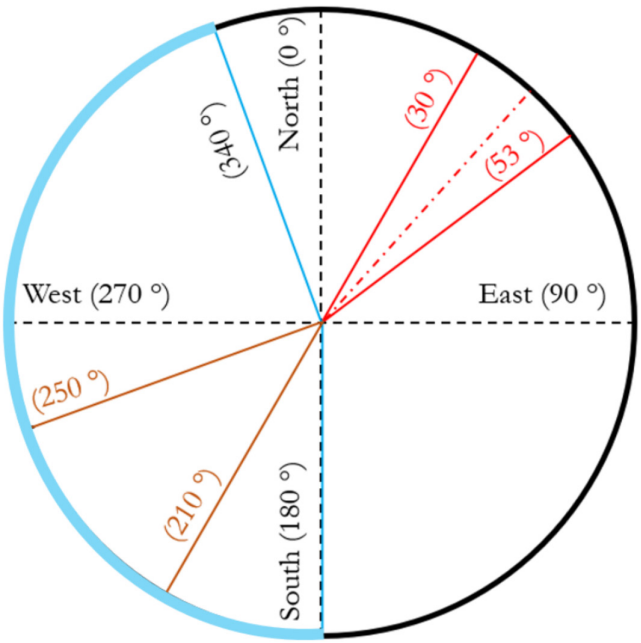

FIGURE 4 | A compass plot denoting the undisturbed wind sector (in blue), the prevailing wind sector (in brown), and scanning LiDAR azimuthal sector (in red).

The scanning LiDAR was placed approximately 912 m (7 D) upstream of the wind turbine, and the scan settings are detailed in Appendix A. The azimuthal ranges of the LiDAR are depicted as red lines in Figure 4, where the red center line represents the approximate axis of the wind turbine (for 230° wind direction with zero yaw misalignment). The scan time was approximately 2.8 min, which implies that in a 10-min interval, ideally, three samples were available at every point of the scan.

Four steps were taken for the data processing of the scanning LiDAR data. First, a carrier-to-noise ratio filter was used such that data within the range of − 23 dB and − 3 dB were preserved [40].

Next, as the scope of this study was to assess the mean wake profiles, rather than high-frequency measurements, a data binning

TABLE 1 | Data binning and filtering for wake measurements.

Parameter (at hub height)	Bin limits
Turbulence intensity (TI)	0%–5%, 5%–8.5% and 8.5%–11%
Wind direction	220°–250°
Wind speed	6–11 m/s, in steps of 1 m/s

and averaging step was taken. The data binning was quantified by different inflow conditions of wind direction, wind speed, and turbulence intensity levels, all based on 10-min averaged values. As mentioned previously, a ground-based LiDAR was used to assess the inflow conditions for the quantification of the wake analysis in various bins. However, given that it is not trivial to accurately measure the turbulence by a LiDAR [41], a metereological mast 1 km east of RWT was utilized to measure turbulence intensity at 80 m close to the RWT hub height of 110 m. The parameters of data binning are listed in Table 1.

Here, the turbulence intensity TI is defined as the ratio of the standard deviation of fluctuating wind velocity σ_U to the mean wind speed $\bar{U}$ at hub height, applied to 10-min samples. The sector of 230°–250° provides the most samples given the prevailing wind sector, and has (theoretically) less uncertainty in retrieving wind components from the LiDAR output of line of sight or radial wind speed. This sector is also chosen because it allows for wake capture up to approximately 5D downstream. Furthermore, the field test wake analysis results of the baseline configuration are presented for the period from 25-11-2022 to 23-01-2023, to ensure that wake analysis comparisons were performed for similar atmospheric conditions between the baseline and retrofitted configuration. During the winter months, it was found that the prevailing atmospheric stability conditions were either neutral, stable, or very stable, while unstable conditions were hardly present. Determination of the atmospheric stability was based on the bulk Richardson number [42] atmospheric stability analysis using bins established in [43].

Additional filtering was applied to remove periods of strong gusts in order to improve the accuracy and reliability of the binned data. For this, the power law exponent and the aerodynamic performance of the wind turbine were assessed. The difference in power law wind shear exponents was maintained within ± 0.1 for comparing the two configurations. The aerodynamic performance check considered rotor power, rotor speed, and blade pitch values. Samples were filtered out if the variation of these parameters was outside acceptable ranges.

A third step in the processing of the scanning LiDAR data was Gaussian process regression on the bin-averaged dataset. This step was utilized in cases where a complete wind field visualization was lacking. The ARD (automatic relevance determination) Matérn 3/2 Kernel was used in this work using the "fitrgp" function of MATLAB [44]. The Matérn 3/2 kernel is a standard kernel for environmental data, and the ARD Matérn 3/2 kernel resulted in a good match with observations. Gaussian process regression has been utilized in previous research [40, 45] for high-frequency LiDAR measurements. The use of Gaussian process regression helped to smooth the dataset (in addition to the reliable interpolation of small gaps in the data), given the inherent standard error in the bin-averaged scanning LiDAR dataset.

Finally, the wind component retrieval step was taken since a LiDAR measures only the radial component of wind speed. Filtering out the wind sectors where the measurements were affected by nearby wakes from other turbines made the retrieval of the necessary wind components less challenging. Using geometric relations (and assuming the LiDAR probe volume to be negligible), the following equation was used to write the radial velocity in terms of the u, v, w components and the scanning LiDAR's azimuth (ψ) and elevation (θ) as follows:

$$V_r = u \sin\psi \cos\theta + v \cos\psi \cos\theta + w \sin\theta \tag{1}$$

This equation follows from Figure A1, where positive is taken as rotation clockwise from north. The elevation is 0° in the horizon and increases towards zenith in the vertical plane. The horizontal wind speed V_h and the wind direction α can be determined as follows:

$$V_h = \sqrt{u^2 + v^2} \tag{2}$$

$$\alpha = \arctan \frac{u}{v} \tag{3}$$

In order to solve Equation (1) with three unknowns (u, v, w), the Cyclops' dilemma [46] needs to be overcome. Two assumptions were made to solve the equation. First, the w component (vertical) was assumed to be zero, as it can be considered negligible (very low elevation angles [Table A1], leading to a small sine component). Second, it was assumed that the wind direction is homogeneous throughout the wind turbine wake. The wind direction was assumed as the inflow wind direction at the hub height of the wind turbine under study, at approximately 2.2 D upstream. These assumptions lead to the following relations:

$$V_h = \frac{V_r}{\cos(\overline{\alpha} - 180 - \psi)} \tag{4}$$

In the above equation, $\overline{\alpha}$ represents the mean wind direction of the incoming wind. This approach was compared against the commonly used nonlinear least square fitting method [47, 48] and a slightly sophisticated Maximum A Posteriori method (by using UQLab [49]), provided in the appendices.

3.1 | Clarification of Different Wake Plot Types

In the results presented in Section 5, the inflow conditions are depicted for the respective wind speed bins. As outlined in Table 1, the hub height parameters served as the primary criteria for binning. Consequently, the inflow profiles at different heights (measured by ground-based LiDAR profiling) are displayed to identify potential variations in wake behavior caused by differences in wind speed, turbulence intensity, and vertical shear. The results include hub height contours and wake profiles in both horizontal and vertical planes.

The hub height contours were made by combining the points in the range 3 m from the hub height of 110 m, in accordance with the scanning pattern (Figure A3). An estimate of the wake width and the rotor hub line are indicated in the hub height contours with green asterisks. The axial wake profiles are presented for the + 50% blade span location in the lateral direction. These profiles are shown for four different altitudes.

Vertical wake profiles at different altitudes and downstream distances are also shown for the + 50% blade span location in the lateral direction. The + 50% span location was chosen to ensure proper wake capture in all results, up to 5 D downstream. Ideally, these profiles would have been plotted at the ± 75% span line, under the assumption that this point will correspond to the maximum lift and thus would roughly be the point of highest deficits [1, 50]. However, sometimes, this point was found to deviate from the scan pattern or coincide with areas poorly resolved by the LiDAR, such as along the nacelle. To avoid erroneous profiles, the + 50% span was chosen, ensuring uniformity across wind speed bins. It may be noted that the highest deficit points would likely differ for the retrofitted wind turbine.

Lastly, to mitigate bias due to differing wind speed distribution in the bin-averaged data, the wake analysis results are presented for the normalized deficit values. Standard error patches are used to indicate the uncertainty in the field test results. The standard error was defined as $\frac{\sigma}{\sqrt{N}}$, representing the ratio of the standard deviation of measurements to the square root of the number of samples.

The number of scans averaged to present the results is indicated in the contour plots and holds for axial and vertical profiles as well. For example, if the number indicated is 12 scans, then the wake measurements were taken for four 10-min intervals (in line with the scan time shown in Table A1).

4 | Setup and Data Processing of Power and Loads Measurements

The 10-min averaged field measurements of the baseline and the retrofitted configuration were analyzed by means of a data binning and averaging approach. The parameters of interest were chosen as wind turbine power, flapwise blade root bending moment, and tower base fore-aft bending moment. The data binning parameters are shown in Table 2.

TABLE 2 | Binning and filtering criteria for wind turbine power and load measurements.

Parameter (at hub height)	Bin limits
Turbulence intensity (TI)	0%–15%
Wind direction	180°–340°
Wind speed	4–13 m/s, in steps of 1 m/s
Yaw misalignment	−15° to +15°
Power law wind shear exponent (—)	< 0.3
Number of samples (—)	> 4

The power and loads analysis encompassed the entire undisturbed wind field region, unlike the wake analysis bins outlined in Table 1. To enhance the sample size, a broader bin for turbulence intensity was employed, primarily due to the shorter testing period of the retrofitted configuration. The lower and upper limits of the wind speed bins were set to be 1 m/s above the cut-in and the rated wind speed of the wind turbine under investigation. The lower limit was selected to mitigate poor averaging associated with wind turbine startup transients. Additionally, a yaw misalignment filter was applied to ensure a reasonable comparison between configurations, given the wider wind direction bins. Furthermore, a power law wind shear exponent filter was implemented, ensuring values below ≤ 0.3 for both configurations. Lastly, to avoid inadequate averaging of power and loads measurements, a minimum of five 10-min samples per bin was deemed necessary for this study.

5 | Field Test-Based Wake Analysis

To allow for some focus in the wake analysis, two different wind speed bins were considered that are representative of the variation in operational conditions experienced over the full wind speed range. The first corresponds to inflow conditions of 8–9 m/s at hub height, featuring a relatively high tip speed ratio and thrust coefficient, which leads to a less stable and shorter baseline wind turbine wake. This wind speed range corresponded to the wind turbine's partial load region governed by varying rotational speed. The second corresponds to hub height wind speeds of 10–11 m/s, close to the rated wind speed of the wind turbine, which relates to operational conditions at a lower tip speed ratio and thrust coefficient (but roughly maximum thrust in a dimensional sense), which leads to a more stable and longer baseline wind turbine wake. This wind speed range corresponded to the wind turbine's full-load region, governed by varying blade pitch to constrain power production. Turbulence intensity from the meteorological mast was used for data binning (as mentioned in Section 3). However, since the mast is not equipped to measure at multiple heights, this section instead presents turbulence intensity data from the ground-based LiDAR to provide a visualization of turbulence shear across the rotor, acknowledging the previously stated limitations. Lastly, a relatively high turbulence intensity bin (8.5%–11%) was selected for the visualization, to demonstrate the retrofitting to be effective also in case of more turbulent inflow conditions.

Given the influence of wind turbine performance metrics on the velocity deficit in the wake, this analysis also includes a discussion of these metrics over the duration used for wake assessment. Following momentum theory, the thrust coefficient (C_T) allows for estimating the expected changes in the velocity deficit due to changes in C_T, linking it with the axial induction factor $\left(a = \frac{U_\infty - U_{rotor}}{U_\infty}\right)$ in $C_T = 4a(1-a)$. However, the C_T was not directly available from the measurements. Thus, a multi-step approach was employed to get an estimate of the ΔC_T between the configurations. This was done primarily using the dynamic pressure normalized tower fore-aft and flapwise blade root bending moments M_b, and assuming $\Delta C_T \propto \Delta \frac{M_b}{\frac{1}{2}\rho U^2}$. The air-density, ρ was evaluated using the ideal gas law with measured

atmospheric pressure and temperature as input. Next, one can utilize the momentum theory relation of $C_T = 4a(1-a)$, where the axial induction factor is estimated from measurements of a forward-facing nacelle-based LiDAR (not detailed in this study, for brevity and due to confidentiality), to determine C_T for a specific case. Then, using $\Delta C_T \propto \Delta \frac{M_b}{\frac{1}{2}\rho U^2}$, the corresponding Δa could be evaluated, and an estimate could be made for the expected change in velocity deficit due to ΔC_T between the configurations. These differences in performance metrics are discussed in this section for the measurements used for the wake analysis. This estimation is believed to isolate the impact of the retrofitted configuration on wind turbine wake recovery from other factors.

It should be noted that in accordance with the law of large numbers, the general impact of segmented Gurney flaps on turbine performance in the field should be interpreted from Section 6, where a larger sample size enabled a more reliable comparison.

5.1 | Partial Load

First, the results of the wind speed bin of 8–9 m/s are discussed. Figure 5 illustrates the vertical profiles of the incoming wind speed and turbulence intensity.

Here, it can be confirmed that the binning process with wind speed and turbulence intensity, as specified in Table 1, results in similar inflow conditions. A roughly 2 % higher turbulence intensity is noted on the bottom part of the rotor.

The hub height contour in Figure 6 shows the normalized deficit profiles for the baseline and the retrofitted configuration. First, the general wake behavior is observed for this wind speed bin, which is associated with a relatively high wind turbine tip-speed ratio and a high thrust coefficient, leading to increased turbulence in the wake. In line with this operating condition, due to the high induction factor, a high deficit (about 60 %) is seen in the wind turbine wake. The measured velocity deficit is close to the deficit corresponding to operation at the Betz limit. Such observations have also been made in previous studies [50, 51]. Another observation that can be made is that the wake in the retrofitted configuration appears to be thinner compared to the baseline configuration.

Before comparing the quantitative results between the baseline and retrofit, the turbine performance metrics resulting from the binning were examined, as these could lead to different wake characteristics. Using the methodology detailed in the introduction of this section, it was found that in the samples used for this wake analysis bin, the retrofitted configuration had a 1.5% lower thrust coefficient than the baseline configuration. Using the theoretical momentum curve, the 1.5% decrease in thrust coefficient can be translated to a 2.2% reduction of axial induction at this operating point.

The normalized axial wake deficit profiles shown in Figure 7a provide more insight into the wind turbine wake of the two

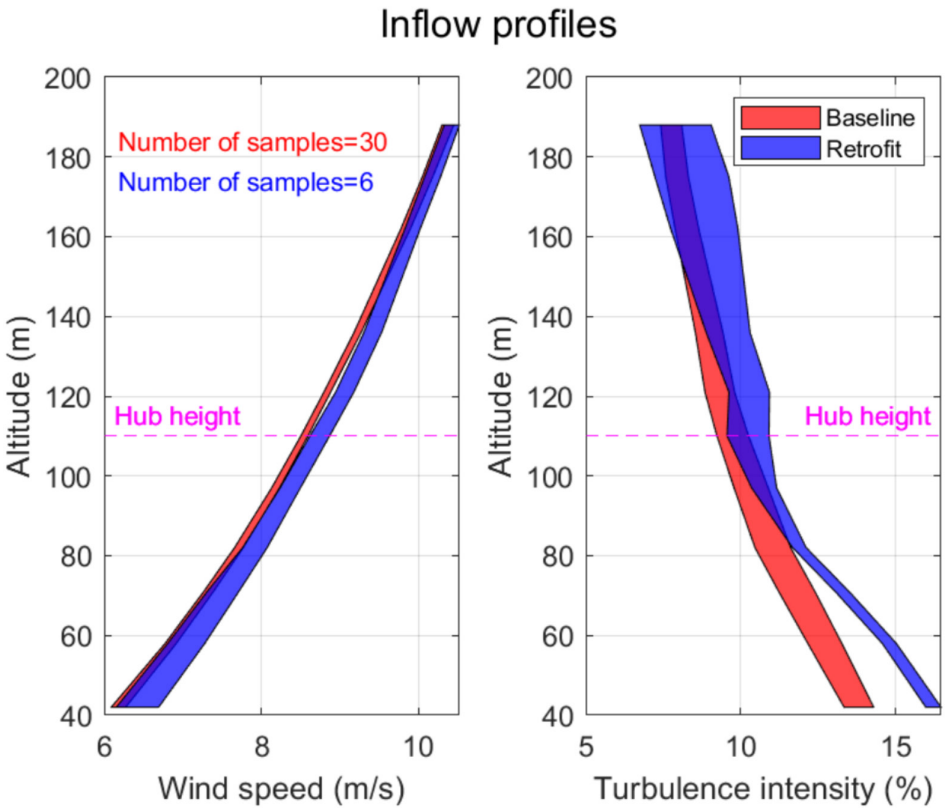

FIGURE 5 | Inflow profiles of wind speed and turbulence intensity for the 8 m/s < $U_{\infty,hub}$ < 9 m/s wind speed bin. The patches indicate one time the standard error of the mean, on each side. WGF and WOGF indicate with Gurney flaps and without Gurney flaps, respectively.

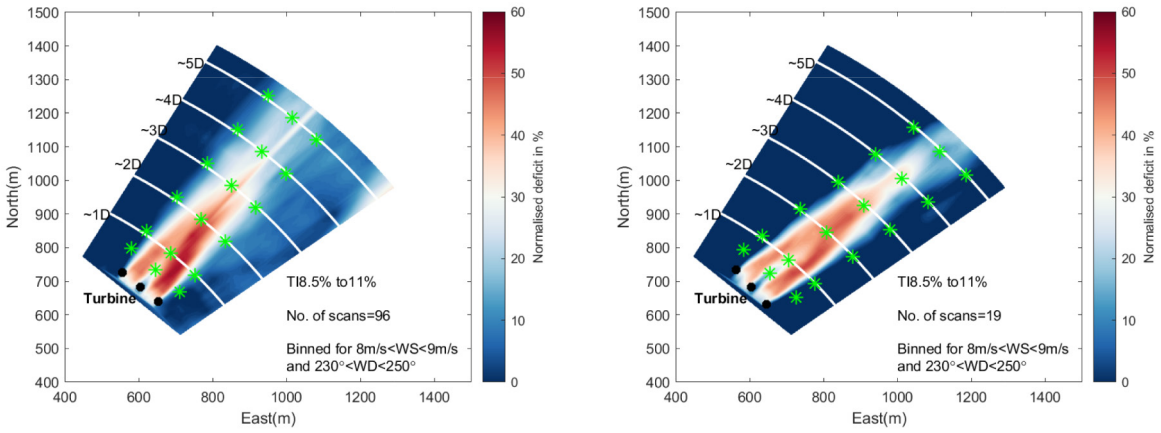

(a) Baseline (without Gurney flaps), in high turbulence intensity inflow

(b) With Gurney flaps, in high turbulence intensity inflow

FIGURE 6 | Wake visualization at hub height for the 8 m/s < $U_{\infty,hub}$ < 9 m/s wind speed bin. The green asterisks represent the assumed 1.5 D wake width and the rotor hub line.

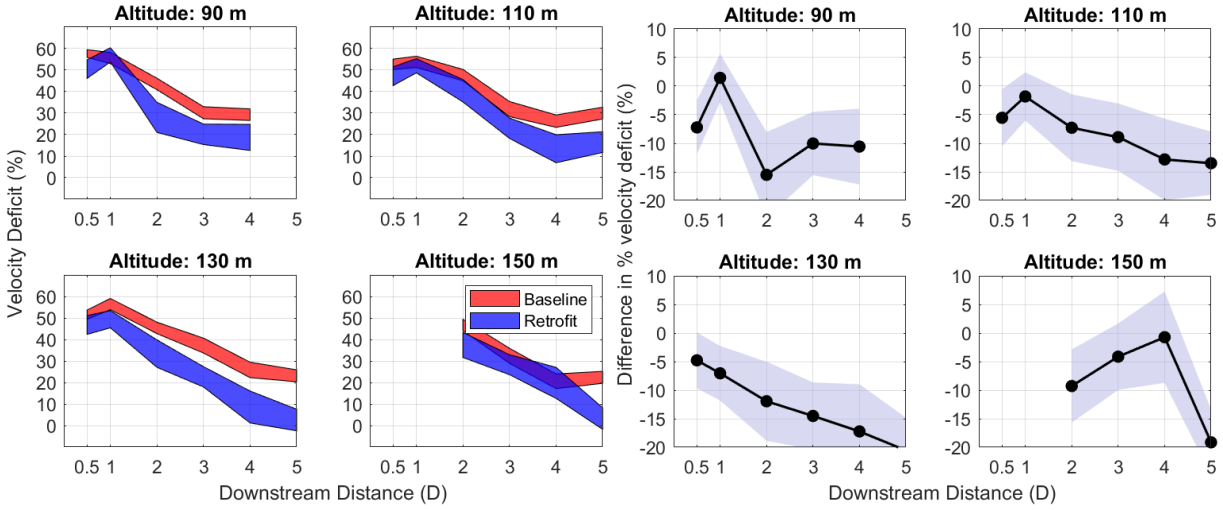

(a) Velocity deficits in the baseline and retrofitted configuration wake

(b) Difference in the velocity deficits of the retrofitted and baseline configuration wake

FIGURE 7 | Axial wake deficit profiles for the 8 m/s < $U_{\infty,hub}$ < 9 m/s wind speed bin at different downstream distances. The profiles are normalized with U_{∞} at hub height. The patches indicate one time the standard error of the mean, on each side.

configurations. The axial profiles indicate a faster recovery for the retrofitted configuration at the different altitudes and downstream distances. The peaks for the deficit appear around 1 D downstream, after which both configurations show a recovery. This peak deficit is expected because of the relaxation of pressure gradients [52, 53]. Further downstream, the turbulent mixing prevails, and the wake recovery is influenced by the ambient turbulence. However, the retrofitted configuration indicates a faster wake recovery, albeit with higher standard errors. The wake of the retrofitted configuration features a steeper wake recovery slope, as in a faster recovery from the region 1 D to 3 D downstream, in comparison to the baseline configuration wake. This observation indicates the earlier tip-vortex wake breakdown in the retrofitted configuration wake in this partial load region of turbine operation. The differences in the deficits shown in Figure 7b indicate a reduction of near-wake deficit by 5%–8% and up to 15% reduction is observed at 5 D downstream.

The normalized vertical wake deficit profiles in Figure 8a also indicate the same trend and the differences between the configurations are presented in Figure 8b. It can be observed that at the 0.5 D downstream region close to the rotor, lower deficits are present for the retrofitted configuration, and the wake profile shapes for the two configurations are similar. In the 1 D and 2 D downstream region, there appears to be an indication of a steeper slope in the wake of the retrofitted configuration and a trend for a double Gaussian wake profile. Despite the expected 2.2% reduced deficit in the retrofitted configuration wake due to the lower induction factor, overall, significantly larger differences in deficits are observed in the retrofitted configuration, hence, mainly attributed to the segmented Gurney flaps.

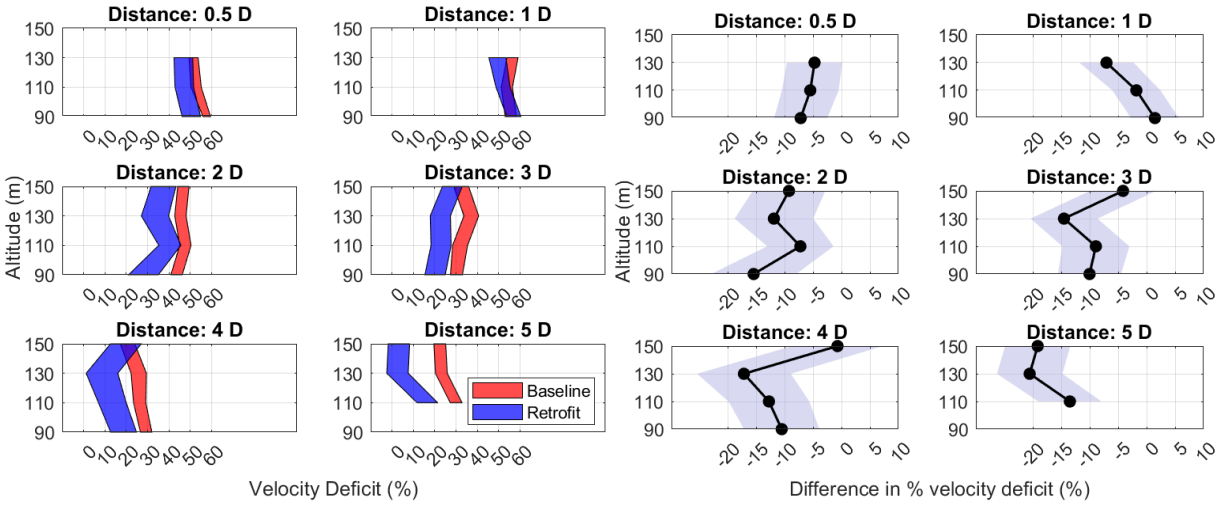

(a) Velocity deficits in the baseline and retrofitted configuration wake

(b) Difference in the velocity deficits of the retrofitted and baseline configuration wake

FIGURE 8 | Vertical wake deficit profiles for the 8 m/s< $U_{\infty,hub}$ < 9 m/s wind speed bin at different downstream distances. The profiles are normalized with U_∞ at hub height. The patches indicate one time the standard error of the mean, on each side.

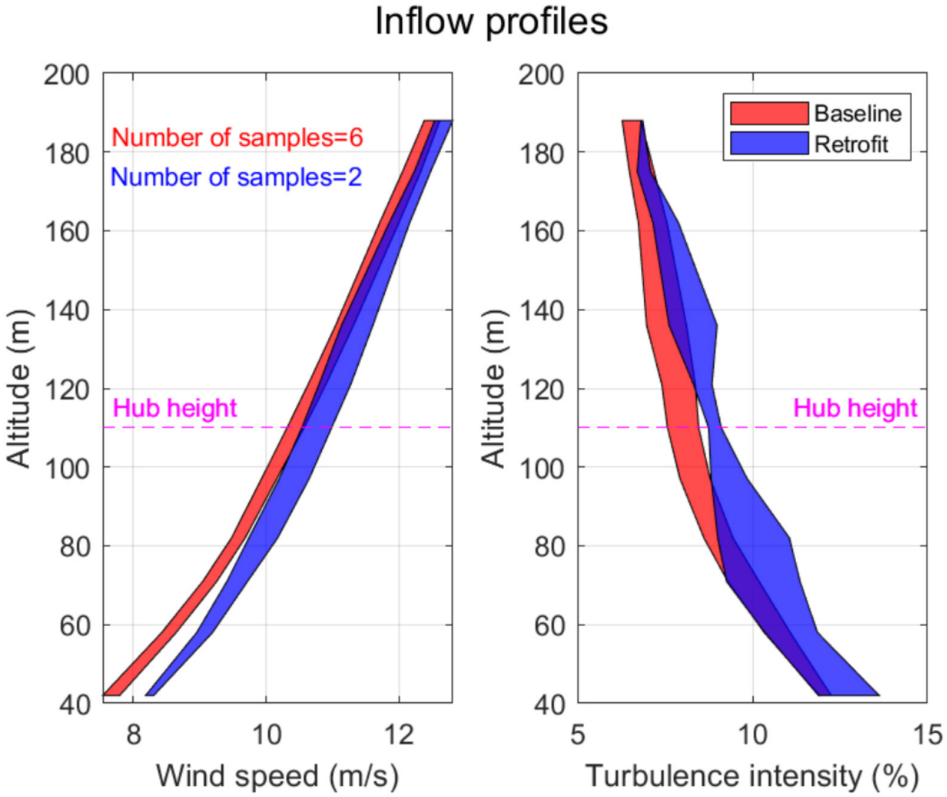

FIGURE 9 | Inflow profiles of wind speed and turbulence intensity for the 10 m/s < $U_{\infty,hub}$ < 11 m/s wind speed bin. The patches indicate one time the standard error of the mean, on each side.

5.2 | Rated Conditions

Next, the 10- to 11-m/s wind speed bin results are discussed. The inflow conditions are shown in Figure 9. The wind speed and turbulence difference are within the bin width for both configurations, but a slightly higher value of turbulence is evident for the retrofitted configuration. However, the differences in turbulence variation with height are lower than the previously discussed bin.

In this wind speed bin, the wind turbine operates at the highest thrust in dimensional form but a lower thrust coefficient and tip speed ratio than the previous wind speed bin. The effect of this condition is reflected in the hub height contour. As expected,

at such operating conditions, the turbulence in the near wake would be limited [54, 55], leading to a much longer wake as clearly seen in Figure 10a.

In comparison to the previous wind speed bin, the deficits in this wind speed bin are lower than the 8–9 m/s wind speed bin, due to the lower thrust coefficient. Furthermore, from Figure 10b, a chaotic wake is seen in the retrofitted configuration. This is hypothesized mainly to be caused by the low number of samples for the averaging but also the increased turbulence in the wake upon the addition of segmented Gurney flaps could have contributed.

Similar to the 8- to 9-m/s bin, the turbine performance metrics resulting from the binning were compared. It was found that the retrofitted configuration featured a higher axial load (from flapwise blade root moment and tower base fore-aft moment). However, the average wind speed and air density in this bin were also higher for the two available samples of the retrofitted configuration wake compared to the baseline. Once again, utilizing the methodology discussed in the introduction of this section, it was estimated that the retrofitted configuration was operating at a 5% lower thrust coefficient. Using the theoretical momentum curve, the 5% decrease in thrust coefficient can be translated to a 6.1% reduction of axial induction at this operating point.

Further quantitative insights into the wake differences are enabled by the axial wake profiles shown in Figure 11a. An enhanced wake recovery is observed in the retrofitted configuration at all heights and downstream distances. The extremely stable structure of the tip vortex for this operational condition would imply a pronounced effect of the segmented Gurney flaps. This is also seen in the vertical wake deficit profiles shown in

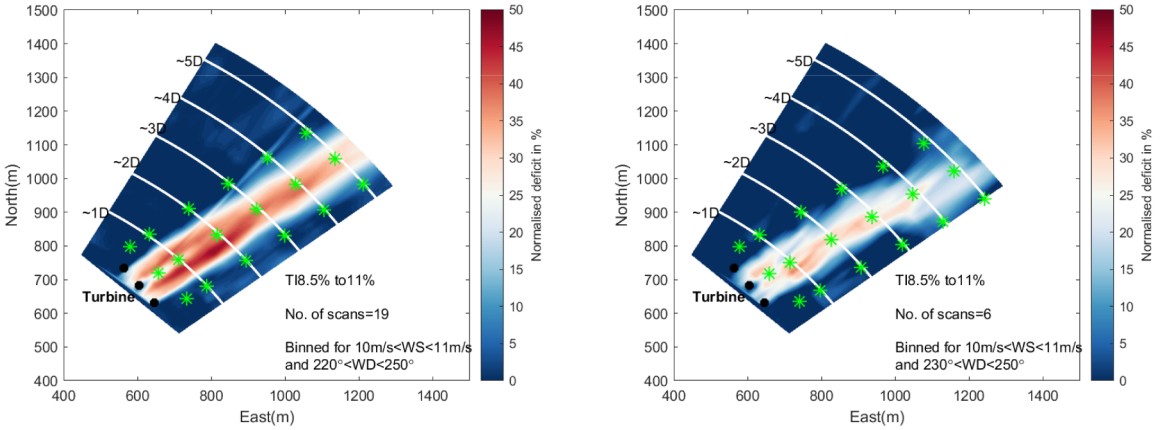

(a) Without Gurney flaps, in high turbulence intensity inflow

(b) With Gurney flaps, in high turbulence intensity inflow

FIGURE 10 | Wake visualization at hub height for the 10 m/s< $U_{\infty,hub}$ < 11 m/s wind speed bin. The green asterisks represent the assumed 1.5 D wake width and rotor hub line.

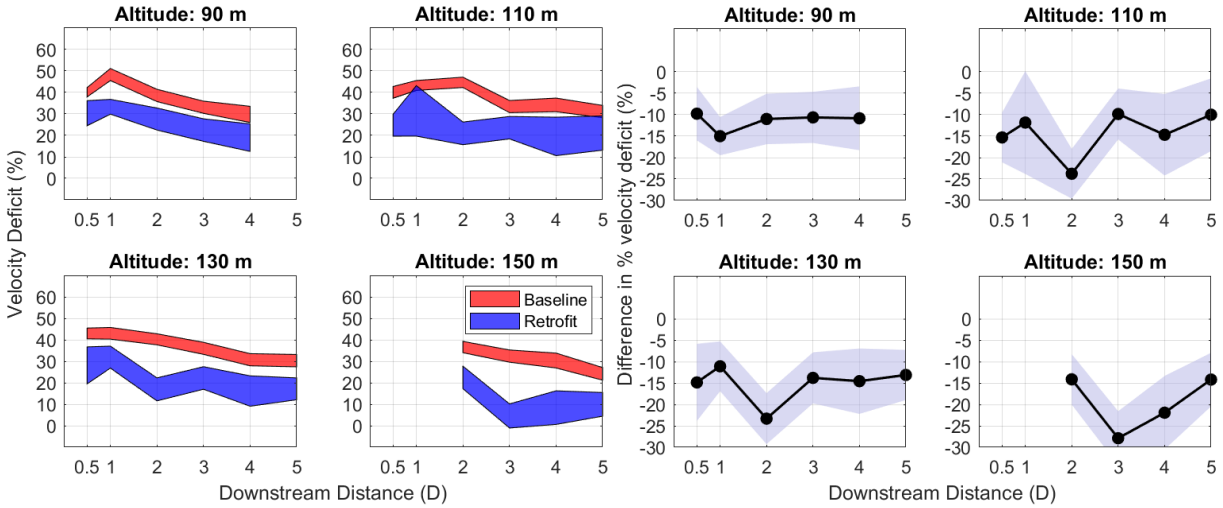

(a) Velocity deficits in the baseline and retrofitted configuration wake

(b) Difference in the velocity deficits of the retrofitted and baseline configuration wake

FIGURE 11 | Axial wake deficit profiles for the 10 m/s < $U_{\infty,hub}$ < 11 m/s wind speed bin at different altitudes. The profiles are normalized with U_{∞} at hub height. The patches indicate one time the standard error of the mean, on each side.

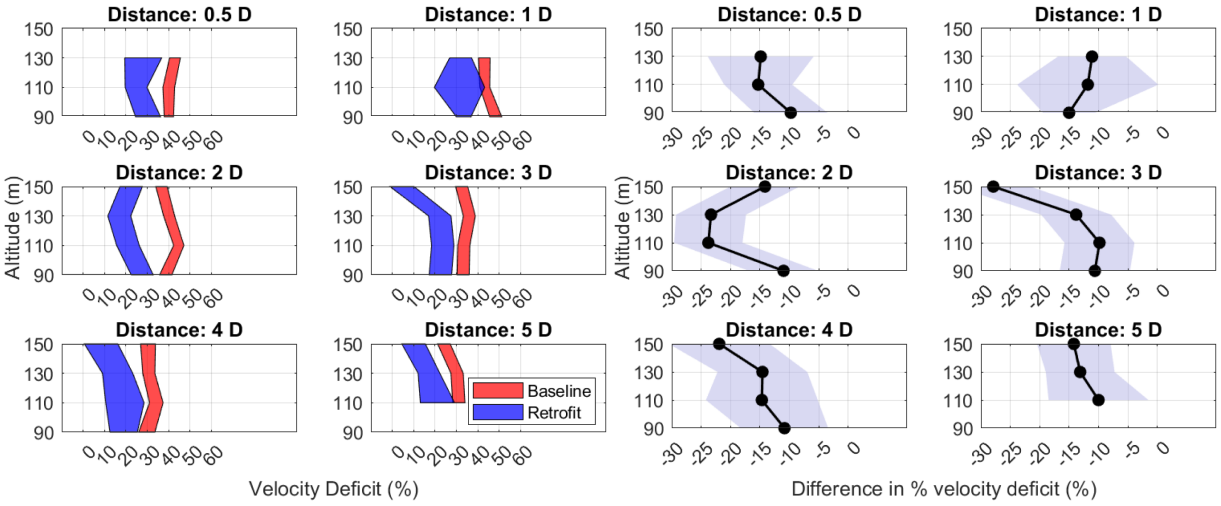

(a) Velocity deficits in the baseline and retrofitted configuration wake

(b) Difference in the velocity deficits of the retrofitted and baseline configuration wake

FIGURE 12 | Vertical wake deficit profiles for the 10 m/s $< U_{\infty,hub} <$ 11 m/s wind speed bin at different downtream distances. The profiles are normalized with U_∞ at hub height. The patches indicate one time the standard error of the mean, on each side.

Figure 12a. It can be observed that up to 15% reduction in deficit is seen at 5 D downstream distance (Figure 12b).

The fact that a reduced wake deficit (larger than the one expected from the discussed reduction in axial induction for the sub-set of data used for wake analysis) is already apparent in the near wake at a downstream distance of 0.5 D gives rise to some discussion. After all, the retrofit was designed to improve wake recovery which occurs downstream of the point featuring maximum deficit. Upwind of this region, the wake deficit is assumed to relate to the axial induction in agreement with moment theory. Although measurement uncertainty can not be excluded, it is hypothesized that early mixing due to the turbulators contributes to the measured observation in the near wake.

In summary, great insights into the wind turbine wake were made possible with the field tests conducted in this study. The results indicate a reduction of the velocity deficit by 10% for the retrofitted configuration, at hub height, at 5 D downstream distance. Despite a short measurements campaign, the differences between the configurations largely exceed the standard error. Hence, application of segmented Gurney flaps on wind turbines in the outer rows of a wind farm could potentially improve farm yield. Dedicated farm simulations are recommended to investigate this and further confirm the promising potential of segmented Gurney flaps. First scoping calculations subjecting Horns Rev wind farm using the Farmflow tool [56], inputting the measured wake recovery improvement for the turbines in the outer row, have indicated a promising increase of 0.7% in annual energy production [57].

6 | Power and Loads Analysis

6.1 | Field Measurements

The field measurements of electrical power were used to assess the power coefficient of the baseline and the retrofitted configuration. In Figure 13a, the relative differences in the electrical power generated in the two configurations are shown, and Figure 13b illustrates the relative difference between the electrical power coefficient.

It can observed that while the relative differences in power are large, the normalized power coefficient of the retrofitted wind turbine was found to be at most 4% higher than the baseline but marginal $\leq$ 1% at wind speeds $\geq$ 8 m/s. This power coefficient increase is likely due to the increase in the torque of the wind turbine caused by the lift increase at the wind turbine blade tip region retrofitted with Gurney flaps. As the wind turbine is apparently operating below the Betz optimum, the lift increase results in a power increase as well. Consequently, the rotor speed was observed to increase around 0.5%–1% for a given wind speed in the partial load region and the blade pitch angle by up to 1° in the rated regime. However, the standard errors are in the order of the observed differences; thus, the results should be interpreted with care. It may also be noted that the data-binning for the power and loads measurements was done with a wind shear exponent maximum limit of 0.3 (Section 4) to have a higher sample size, but it comes at the expense of not differentiating effects of atmospheric stability on the wind turbine power production. A more controlled simulation set-up was used to further quantify the differences, detailed later in Figure 16.

Next, the flapwise blade root bending moment was assessed, which is shown in Figure 14a. A general increase in flapwise bending moment up to 5% is observed for the retrofitted configuration, depending on wind speed. The outlier in the 7–8 m/s wind speed bin was investigated, and it was found that the average wind speed for the retrofitted configuration was lower by 0.4 m/s. To counter this bias, a normalization of the flapwise blade root bending moment was done with the dynamic pressure, as shown in Figure 14b, where it can be observed that the relative differences are lower and similar to C_p, marginal at wind speeds $\geq$ 8 m/s. Moreover, it can be seen in Figure 14c that the percentage standard errors are high due to the low number of samples, leading to uncertainty in the accurate estimation of the effect

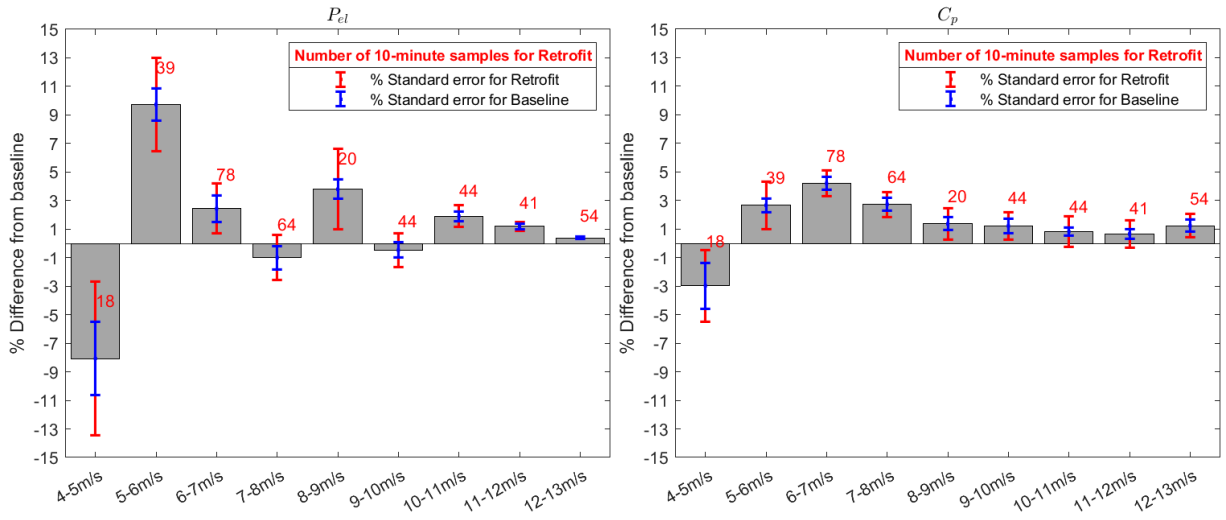

(a) Electrical power generated (b) Electrical power coefficient

FIGURE 13 | Relative difference of power performance metrics, from baseline. The error bars denote the standard error as a percentage of the mean.

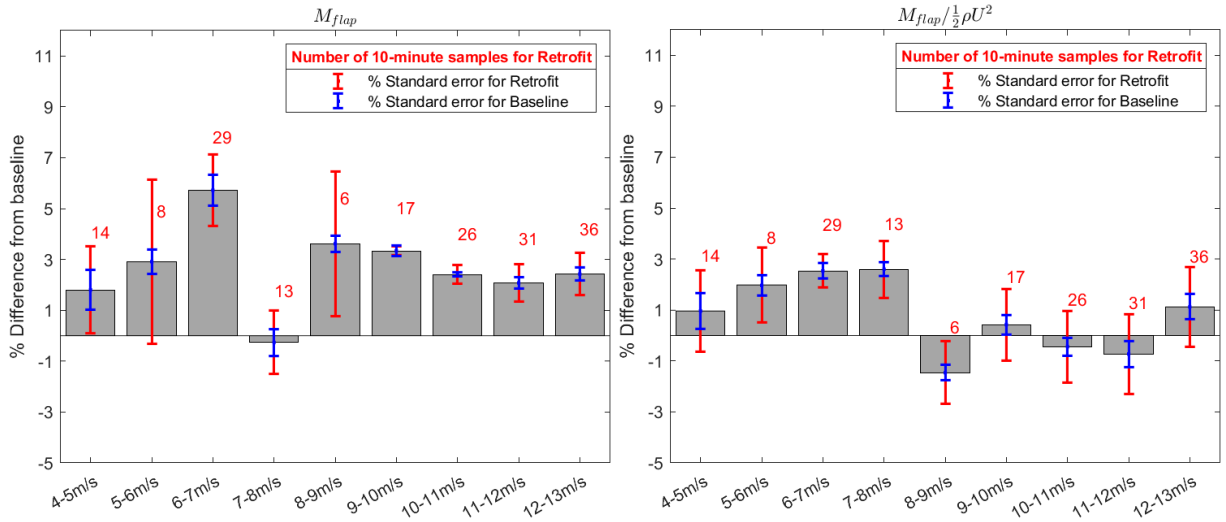

(a) Blade root flapwise bending moment (b) Blade root flapwise bending moment, normalized with dynamic pressure

FIGURE 14 | Relative difference of loads, from baseline. The error bars denote the standard error as a percentage of the mean.

of segmented Gurney flaps on the wind turbine flapwise bending moment. A closer look at the tower base fore-aft moment measurements revealed a similar trend with increasing values for the retrofitted configuration. As indicated in Figure 14, the flapwise bending moment signal for the retrofitted configuration had only six samples for some of the bins, while for the baseline configuration about 30 times more samples were recorded. Because of such anomalies, caution should be exercised when drawing conclusions from the field test turbine performance analysis.

6.2 | Simulations

To further study the effect of retrofitting on turbine performance, simulations were set up in accordance with the IEC normal turbulence model (NTM), and the cut-in to cut-out wind speeds were simulated using TurbSim [58] generated wind fields. The Delft Research controller [59] was used for the dynamic simulations, which were run for 660 s, the first 60 s of which were not included in the result analysis. The simulations were run with a time step of 5 ms. The setup and validation of the simulation setup are provided in [38].

First, the angle of attack on the wind turbine blade tip was assessed. The angle of attack across the spanwise positions corresponding to Gurney flaps ranged from roughly 2°–0° in the 4–10 m/s wind speed range and then decreased to roughly $-8°$ to $-12°$ towards the 25 m/s wind speed range. Based on the available literature (e.g., [34]), it is evident that Gurney flaps affect the lift coefficient within a conventional angle of attack range from approximately $\approx -8°$ to $\approx 12°$. Therefore, at very high wind

speeds, the impact of Gurney flaps will be more evident as drag rather than lift.

Regarding the difference in the angle of attack with respect to the baseline configuration, it was found that the retrofitted configuration has a lower local angle of attack. This is because of the increased lift and the corresponding rotor induction, the effect of which is illustrated in Figure 15.

The reduction in angle of attack is observed to be higher until the rated wind speed of approximately 11 m/s. As will be explained below, this change will likely be the cause of the trends observed in the power and loads of the retrofitted wind turbine.

Next, with regard to the electrical power, a general increase was observed below the rated wind speed. Above the rated wind speed, the controller curtailed the power in both configurations as per a torque-speed look-up table in accordance with the 3.8-MW research wind turbine specifications. The difference across all wind speed bins is shown in Figure 16a. The magnitude of the relative power difference is found to be lower in the simulations. Although the cause for this discrepancy is unclear, it could partly originate from the controller in the simulations not accurately replicating the field wind turbine controller. Nevertheless, the lower end of the relative differences seen in measurements shows a reasonable match with the simulations.

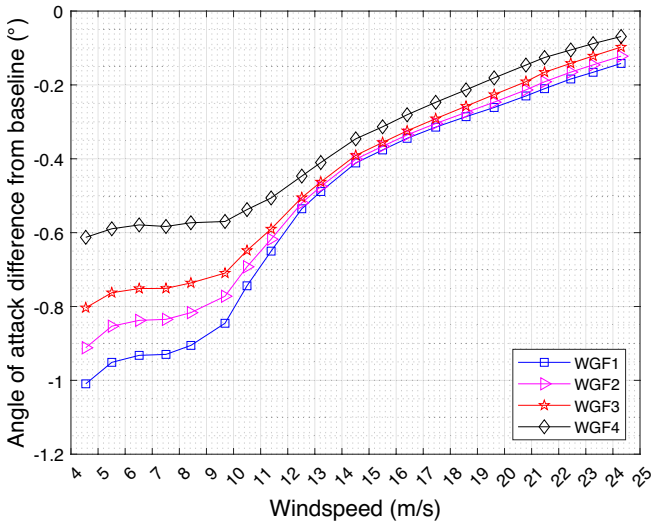

FIGURE 15 | Simulated difference in angle of attack from baseline at the different Gurney flap positions. WGF1–WGF4 represent the four different spanwise Gurney flap positions along the wind turbine blade tip as shown in Figure 3b.

The simulation results of electrical power were used to estimate the impact of the segmented Gurney flaps on annual energy production (AEP). From cut-in to cut-out wind speed range, the AEP estimate was made with the formulation shown below.

$$AEP = 8766 \int_{U_{cut-in}}^{U_{cut-out}} P_{el}(U) f_{prob}(U) dU \tag{5}$$

In the above equation, 8766 is the number of hours in a year. P_{el} represents the electric power, and $f_{prob}(U)$ represents the probability of the wind speed obtained from the Weibull distribution for the test site at hub height. dU represents the size of the wind speed bins, here used in steps of 1 m/s. This results in an increase in annual energy production of the retrofitted wind turbine by roughly $+0.2\%$.

Next, the flapwise blade root moment was found to increase mainly in the partial load region, after which only a minimal increase in rotor thrust was observed (Figure 16b). This is associated with the reduced angle of attack in this region, at which the effect of the Gurney flaps on the lift coefficient diminishes. With this discussion on some of the important parameters indicating the structural effects of the tip Gurney flaps, it is clear that, although minimal, the structural loads will increase at all wind speeds for the retrofitted wind turbine. It is worth mentioning that the trend observed in the simulation results aligns well with the measurements, suggesting that the simulations give a good sense of the impact of segmented Gurney flaps on wind turbine power and loads. As to the absolute values, an adequate agreement has been observed. For instance, the lower end of the power increase in measurements ranges between 0% and 1%, and in simulations it is approximately 0.5%. The average increase in blade flapwise bending moments is about 3% in measurements and roughly 2% in simulations, for wind speeds from 4 to 12 m/s.

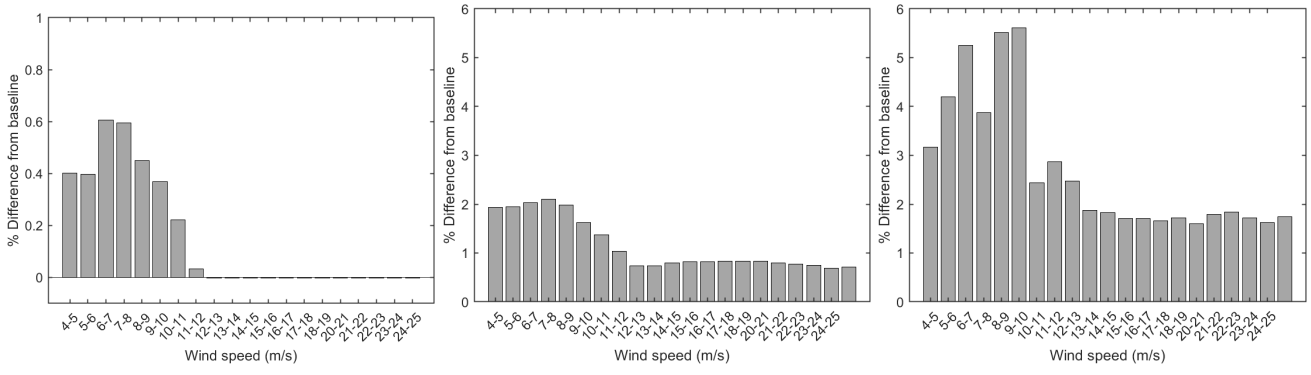

(a) Electrical power comparison

(b) Flapwise bending moment comparison

(c) Damage equivalent flapwise bending moment comparison for a Wöhler exponent of 12.

FIGURE 16 | Relative difference of turbine performance metrics, from baseline.

To assess the long term effect of this increase in structural loads a fatigue analysis was conducted. In this study, a fatigue assessment based on the damage equivalent load formulation (corrected for mean stress) of [60] was used with the input of the blade root flapwise bending moment spectrum. Here, a Wöhler exponent of 12 was used to present composite material as used for the blades. In Figure 16c, it can be observed that the damage equivalent flapwise blade root bending moment is higher for the retrofitted wind turbine. The peaks occur in the partial load region, attributed to the higher lift curve slope in this region. Upon incorporating the Weibull distribution of wind speed into the damage equivalent flapwise bending moment differences, roughly a 5% increase is found after the Weibull weighting.

7 | Conclusions and Recommendations

The objective of this research was to assess the effectiveness of employing segmented Gurney flaps in the region near the wind turbine blade tips. The focus was on improving wake recovery and analyzing the effects on both the retrofitted wind turbine power and loads.

The main hypothesis behind the use of segmented Gurney flaps for faster wake recovery was to destabilize the system of helical vortices. This would be induced by the resulting jagged lift and circulation distribution on the wind turbine blade tip, which leads to additional vortices shed from the edges of the Gurney flap, resulting in earlier mutual inductance of the vortex filaments. Additionally, the higher pressure drag due to the Gurney flap was hypothesized to increase turbulence in the wake. Four Gurney flaps (designed as a wedge) were attached to the outboard 7% span of each blade of a 3.8-MW research wind turbine.

Field measurements using a scanning LiDAR were quantified with bins of wind direction, wind speed, and turbulence intensity using measurements from a ground-based profiling LiDAR. The scanning LiDAR was used to scan a sector up to 5D downstream at different altitudes in a sector which was approximately 20° wide. The measurements were binned and averaged for wake analysis.

Enhanced wake recovery was observed for the retrofitted configuration, generally at all downstream distances and altitudes. The improved wake recovery was not only observed for high tip speed ratios and thrust coefficients but also confirmed for the lower tip speed ratios and thrust combinations above rated conditions. The retrofitted configuration results indicate lower averaged deficits by roughly 10% at hub height, at a downstream distance of 5D. However, the retrofitted configuration results were associated with a higher standard error and therefore the results should be interpreted with care.

Application of segmented Gurney flaps on wind turbines in the outer rows of a wind farm could potentially improve farm yield. More sophisticated farm simulations are recommended to investigate this and further confirm the promising results of the first scoping calculations, indicating a potential increase of 0.7% in annual energy production for a typical wind farm layout.

The 10-min averaged field measurements of the wind turbine power and loads were used to assess the impact of the retrofitting. A limited increase in power and loads was found. However, high standard errors were noted in the measurement data. Hence, a controlled and validated aero-elastic simulation set-up was used for further insights into the impact of segmented Gurney flaps on the 3.8-MW research wind turbine. An AEP increase of roughly 0.2% with an increase in the damage equivalent flapwise bending moment at most by roughly 5%, around the partial load region of the wind turbine, was observed.

This makes segmented Gurney flaps a potential promising add-on to wind turbine blades to promote enhanced wake recovery. Recommendations to further promulgate the use of Gurney flaps are related to future field tests and future research on these devices. Longer field tests, around 2 months for each configuration, will allow for improved validation of the enhanced wake recovery. Future studies could also investigate other sources of measurement uncertainties when using a scanning LiDAR and adopt a dynamic CNR-based filtering instead of the CNR threshold-based filtering. The power and loads of a downstream wind turbine or in a full farm setting could be assessed in a future study to further quantify the results. Highly resolved actuator line modeling based Large eddy simulations (with optimal Gaussian kernel width) could be used to assess the velocity profiles with various wind speed and turbulence intensity conditions. Such a study could also be utilized to further optimize the design and spacing of the segmented Gurney flaps on the blade, as the velocity profiles can be assessed in such simulations. Finally, for operation on land, the noise of the devices will have to be reduced. This is, however, less relevant for offshore operations.

Author Contributions

N.D. conducted the analysis presented here as a part of his master's thesis and prepared the first draft of the manuscript. K.B. coordinated the research campaign. K.B. and E.B. acted as supervisors from TNO and aided in the revision. W.B. and W.Y. acted as supervisors from TU Delft.

Funding

This research has been co-financed with Topsector Energiesubsidie from the Dutch Ministry of Economic Affairs under grant no. TEHE119018.

Conflicts of Interest

The authors declare no conflicts of interest.

Data Availability Statement

LiDAR measurement data can be shared on request. Turbine model and measurement data are not available in the public domain.

References

1. L. J. Vermeer, J. N. Sørensen, and A. Crespo, "Wind Turbine Wake Aerodynamics," *Progress in Aerospace Sciences* 39, no. 6–7 (2003): 467–510, https://doi.org/10.1016/S0376-0421(03)00078-2.

2. L. E. M. Lignarolo, "On the Turbulent Mixing in Horizontal Axis Wind Turbine Wakes," 2016, https://doi.org/10.4233/UUID:057FA33F-82A3-4139-BEB8-53F184CD1D57.

3. J. Schepers, "Engineering Models in Wind Energy Aerodynamics: Development, Implementation and Analysis Using Dedicated Aerodynamic Measurements," 2012, https://doi.org/10.4233/UUID:92123C07-CC12-4945-973F-103BD744EC87.

4. K. Boorsma, "Heat and Flux—Analysis of Field Measurements," tech. rep., Energieonderzoek Centrum Nederland (ECN), 2012.

5. J. Wang, C. L. Bottasso, and F. Campagnolo, "Wake Redirection: Comparison of Analytical, Numerical and Experimental Models," *Journal of Physics: Conference Series*. 753, no. 3 (2016): 032064, https://doi.org/10.1088/1742-6596/753/3/032064.

6. D. Dilip and F. Porté-Agel, "Wind Turbine Wake Mitigation Through Blade Pitch Offset," *Energies* 10, no. 6 (2017): 757, https://doi.org/10.3390/EN10060757.

7. P. M. Gebraad, P. A. Fleming, and J. W. Van Wingerden, "Comparison of Actuation Methods for Wake Control in Wind Plants," in Proceedings of the American Control Conference, 2015, https://doi.org/10.1109/ACC.2015.7170977.

8. J. Bartl and L. Sætran, "Experimental Testing of Axial Induction Based Control Strategies for Wake Control and Wind Farm Optimization," *Journal of Physics: Conference Series*. 753, no. 3 (2016): 032035, https://doi.org/10.1088/1742-6596/753/3/032035.

9. C. H. Westergaard, "Method for Improving Large Array Wind Park Power Performance Through Active Wake Manipulation Reducing Shadow Effects," 2012.

10. J. Goit and J. Meyers, "Optimal Control of Energy Extraction in Wind-Farm Boundary Layers," *Journal of Fluid Mechanics* 768 (2015): 5–50, https://doi.org/10.1017/jfm.2015.70.

11. W. Munters and J. Meyers, "Towards Practical Dynamic Induction Control of Wind Farms: Analysis of Optimally Controlled Wind-Farm Boundary Layers and Sinusoidal Induction Control of First-Row Turbines," *Wind Energy Science* 3, no. 1 (2018): 409–425, https://doi.org/10.5194/WES-3-409-2018.

12. J. Frederik, R. Weber, S. Cacciola, et al., "Periodic Dynamic Induction Control of Wind Farms: Proving the Potential in Simulations and Wind Tunnel Experiments," *Wind Energy Science* (2019), https://doi.org/10.5194/wes-2019-50.

13. J. A. Frederik, B. M. Doekemeijer, S. P. Mulders, and J-W. van Windergen, "The Helix Approach: Using Dynamic Individual Pitch Control to Enhance Wake Mixing in Wind Farms," *Wind Energy* 23, no. 8 (2020): 1739–1751, https://doi.org/10.1002/we.2513.

14. X. Huang, S. M. Alavi Moghadam, P. S. Meysonnat, M. Meinke, and W. Schröder, "Numerical Analysis of the Effect of Flaps on the Tip Vortex of a Wind Turbine Blade," *International Journal of Heat and Fluid Flow* 77 (2019): 336–351, https://doi.org/10.1016/J.IJHEATFLUIDFLOW.2019.05.004.

15. W. Zhang, Y. Wang, Y. Shen, Y. Wang, Y. Xu, and X. Zhang, "CFD Studies of Wake Characteristics and Power Capture of Wind Turbines With Trailing Edge Flaps," *IEEE Access* 8 (2020): 7349–7361, https://doi.org/10.1109/ACCESS.2020.2964620.

16. D. Marten, C. O. Paschereit, X. Huang, et al., "Predicting Wind Turbine Wake Breakdown Using a Free Vortex Wake Code," *AIAA Journal* 58, no. 11 (2020): 4672–4685, https://doi.org/10.2514/1.J058308.

17. A. Van Garrel and E. T. G. Bot, "Rotor Blade for a Wind Turbine, and Wind Turbine Field," 2014.

18. O. Ceyhan Yilmaz and V. J. H. Kalken, "InnoTIP End Report," tech. rep., ECN & LM Wind Power, 2017.

19. F. Mühle, J. Bartl, T. Hansen, M. S. Adaramola, and L. Sætran, "An Experimental Study on the Effects of Winglets on the Tip Vortex Interaction in the Near Wake of a Model Wind Turbine," *Wind Energy* 23, no. 5 (2020): 1286–1300, https://doi.org/10.1002/WE.2486.

20. J. A. C. Kentfield, "Theoretically and Experimentally Obtained Performances of Gurney-Flap Equipped Wind Turbines," *Wind Engineering* 18, no. 2 (1994): 63–74.

21. K. Boorsma and J. G. Schepers, "Rotor Experiments in Controlled Conditions Continued: New Mexico," *Journal of Physics: Conference Series* 753, no. 2 (2016): 022004, https://doi.org/10.1088/1742-6596/753/2/022004.

22. J. Alber, R. Soto-Valle, M. Manolesos, et al., "Aerodynamic Effects of Gurney Flaps on the Rotor Blades of a Research Wind Turbine," *Wind Energy Science* 5, no. 4 (2020): 1645–1662, https://doi.org/10.5194/WES-5-1645-2020.

23. D. T. Y. Nakafuji, C. P. Dam Van, R. L. Smith, and S. D. Collins, "Active Load Control for Airfoils Using Microtabs," *Journal of Solar Energy Engineering* 123, no. 4 (2001): 282–289, https://doi.org/10.1115/1.1410110.

24. C. P. van Dam, D. Y. Nakafuji, C. Bauer, K. Standish, and D. Chao, "Computational Design and Analysis of a Microtab-Based Aerodynamic Load Control System for Lifting Surfaces," 4981 (2003): 28–39, https://doi.org/10.1117/12.478170.

25. A. B. Bach, "Gurney Flaps and Micro-Tabs for Load Control on Wind Turbines," 2016, https://doi.org/10.14279/DEPOSITONCE-5127.

26. R. H. Liebeck, "On the Design of Subsonic Airfoils for High Lift," *Journal of Aircraft* (1976), https://doi.org/10.2514/3.58406.

27. J. J. Wang, Y. C. Li, and K. S. Choi, "Gurney FlapLift Enhancement, Mechanisms and Applications," *Progress in Aerospace Sciences* 44, no. 1 (2008): 22–47, https://doi.org/10.1016/J.PAEROSCI.2007.10.001.

28. S. A. Solovitz and J. K. Eaton, "Dynamic Flow Response due to Motion of Partial-Span Gurney-Type Flaps," *AIAA Journal* 42, no. 9 (2004): 1729–1736, https://doi.org/10.2514/1.1200.

29. C. G. Matalanis and J. K. Eaton, "Wake Vortex Alleviation Using Rapidly Acuated Segmented Gurney Flaps," tech. rep., Flow Physics and Computation Division; Department of Mechanical Engineering, Stanford University, 2007.

30. C. G. Matalanis and J. K. Eaton, "Wake Vortex Control Using Static Segmented Gurney Flaps," *AIAA* 45, no. 2 (2006): 321–328, https://doi.org/10.2514/1.25956.

31. D. R. Troolin, E. K. Longmire, and W. T. Lai, "Time Resolved PIV Analysis of Flow Over a NACA 0015 Airfoil With Gurney Flap," *Experiments in Fluids* 41, no. 2 (2006): 241–254, https://doi.org/10.1007/S00348-006-0143-8/FIGURES/17.

32. J. S. Delnero, J. M. Di Leo, and M. G. Saínz, "Experimental Study of Near and Far Wake Generated by a Gurney Mini Flap in Turbulent Flow," 34th Wind Energy Symposium, 2016, https://doi.org/10.2514/6.2016-0522.

33. D. Holst, A. B. Bach, C. N. Nayeri, C. O. Paschereit, and G. Pechlivanoglou, "Wake Analysis of a Finite Width Gurney Flap," *Journal of Engineering for Gas Turbines and Power*. 138, no. 6 (2016), https://doi.org/10.1115/1.4031709/374189.

34. J. Yang, H. Yang, W. Zhu, N. Li, and Y. Yuan, "Experimental Study on Aerodynamic Characteristics of a Gurney Flap on a Wind Turbine Airfoil Under High Turbulent Flow Condition," *Applied Sciences* 10 (2020): 7258, https://doi.org/10.3390/APP10207258.

35. A. W. Bloy and N. Tsioumanis, "Trailing Edge Wedge Flaps for Wind-Turbine Blades," *Wind Engineering* 21, no. 1 (1997): 39–44.

36. L. S. Hao and Y. W. Gao, "Effect of Gurney Flap Geometry on a S809 Airfoil," *International Journal of Aerospace Engineering* 2019 (2019): 9875968, https://doi.org/10.1155/2019/9875968.

37. J. Jonkman, M. Sprague, et al., "OpenFAST — Wind Research — NREL," 2022.

38. N. S. Dangi, "Segmented Gurney Flaps for Enhanced Wind Turbine Wake Recovery" (MSc thesis, 2023).

39. H. G. Weller, G. Tabor, H. Jasak, and C. Fureby, "A Tensorial Approach to Computational Continuum Mechanics Using Object-Oriented Techniques," *Computers in Physics* 12, no. 6 (1998): 620, https://doi.org/10.1063/1.168744.

40. N. Cassamo, M. Turrini, D. A. J. Wouters, W. van der PA, W. A. Castricum, and J. W. Wagenaar, *Application of Gaussian Processes to Dual-Doppler LiDAR Scanning Measurements for High Frequency Wind Field Reconstruction* (TNO Publications, 2021).

41. A. Sathe, J. Mann, J. Gottschall, and M. S. Courtney, "Can Wind Lidars Measure Turbulence?," *Journal of Atmospheric and Oceanic Technology* 28, no. 7 (2011): 853–868.

42. A. A. Grachev and C. W. Fairall, "Dependence of the Monin-Obukhov Stability Parameter on the Bulk Richardson Number Over the Ocean," *Journal of Applied Meteorology and Climatology* 36, no. 4 (1997): 406–414, https://doi.org/10.1175/1520-0450(1997)036.

43. S. E. Gryning, E. Batchvarova, B. Brümmer, H. Jørgensen, and S. Larsen, "On the Extension of the Wind Profile Over Homogeneous Terrain Beyond the Surface Boundary Layer," *Boundary-Layer Meteorology* 124, no. 2 (2007): 251–268, https://doi.org/10.1007/S10546-007-9166-9.

44. "Mathworks—MATLAB," Fit a Gaussian Process Regression (GPR) Model - MATLAB fitrgp – MathWorks, 2022.

45. C. Stock-Williams, P. Mazoyer, and S. Combrexelle, "Wind Field Reconstruction From Lidar Measurements at High-Frequency Using Machine Learning," *Journal of Physics: Conference Series.* 1102, no. 1 (2018): 012003, https://doi.org/10.1088/1742-6596/1102/1/012003.

46. E. Simley and L. Y. Pao, "LIDAR Wind Speed Measurements of Evolving Wind Fields," 2012.

47. N. Bodini, D. Zardi, and J. K. Lundquist, "Three-Dimensional Structure of Wind Turbine Wakes as Measured by Scanning Lidar," *Atmospheric Measurement Techniques.* 10, no. 8 (2017): 2881–2896, https://doi.org/10.5194/AMT-10-2881-2017.

48. A. Peña, J. Mann, and G. R. Thorsen, *SpinnerLidar Measurements for the CCAV52* (DTU Wind Energy, 2019).

49. S. Marelli and B. Sudret, "UQLab: A Framework for Uncertainty Quantification in Matlab," 2554–2563.

50. M. L. Aitken, R. M. Banta, Y. L. Pichugina, and J. K. Lundquist, "Quantifying Wind Turbine Wake Characteristics From Scanning Remote Sensor Data," *Journal of Atmospheric and Oceanic Technology* 31, no. 4 (2014): 765–787, https://doi.org/10.1175/JTECH-D-13-00104.1.

51. P Van Dorp, "Quantification of Wind Turbine Wake Characteristics From Scanning LiDAR Measurements," 2016.

52. J. F. Ainslie, "Calculating the Flowfield in the Wake of Wind Turbines," *Journal of Wind Engineering and Industrial Aerodynamics* 27, no. 1–3 (1988): 213–224, https://doi.org/10.1016/0167-6105(88)90037-2.

53. B. Sanderse, "Aerodynamics of Wind Turbine Wakes Literature Review," tech. rep., ECN, 2009.

54. N. Troldborg, "Actuator Line Modeling of Wind Turbine Wake" (PhD thesis, Technical University of Denmark), 2009.

55. L. A. Martínez-Tossas, E. Branlard, K. Shaler, et al., "Numerical Investigation of Wind Turbine Wakes Under High Thrust Coefficient," *Wind Energy* 25, no. 4 (2022): 605–617, https://doi.org/10.1002/we.2688.

56. E. Bot and S. Kanev, "Farm Flow, Extensively Validated and Dedicated Model for Wind Farm Control," tech. rep., TNO, 2020.

57. K. Boorsma, N. Dangi, and E. Bot, "Boosting Wind Farm Efficiency: Application of Blade Turbulators," 2024, Bilbao, Spain.

58. B. J. Jonkman and L. Kilcher, *TurbSim User's Guide*, tech. rep. (National Renewable Energy Laboratory, US Department of Energy, 2012).

59. S. P. Mulders and J. W. Van Wingerden, "Delft Research Controller: An Open-Source and Community-Driven Wind Turbine Baseline Controller," *Journal of Physics: Conference Series* 1037, no. 3 (2018): 032009, https://doi.org/10.1088/1742-6596/1037/3/032009.

60. H. B. Hendriks and B. H. Bulder, "Fatigue Equivalent Load Cycle Method," tech. rep., Energy Research Centre of the Netherlands (ECN), 1995.

Appendix A

Scanning LiDAR Pattern

The scanning LiDAR settings are summarized in Table A1, where the azimuth (ψ) and elevation (θ) conventions are defined in Figure A1. Here, LOS denotes the line of sight of the LiDAR.

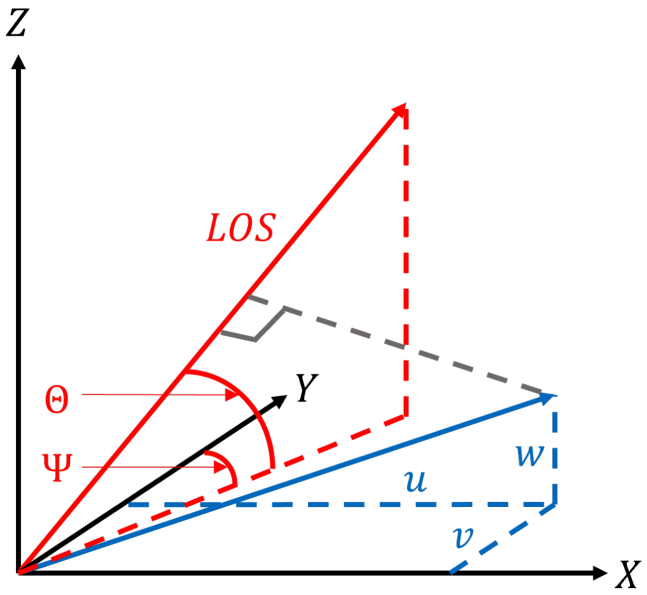

FIGURE A1 | Scanning LiDAR coordinate system.

TABLE A1 | Scanning LiDAR settings.

Parameter	Min.	Max.	Step size	No. of unique points	Time for 1 scan (minutes)	Total no. of points in ideal scan
ψ (°)	30	52.88	0.22	105		
θ (°)	4	7.5	0.5	7	2.8	22,050
Range (m)	900	1625	25	30		

The scope of this pattern was to have enhanced visualization at hub height for the prevailing wind sector. This pattern enabled lowering the standard error of the results because of the relatively fast scan time. Furthermore, the elevation angles were chosen such that sufficient resolution is available for vertical profiles of the wind turbine wake. Overall, the final pattern enabled highly resolved wind turbine wake field measurements, with roughly three full scans in a 10-min interval.

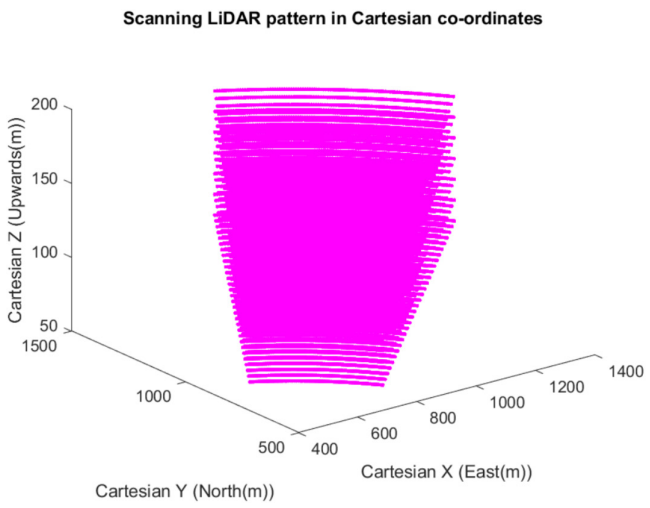

FIGURE A2 | Scanning LiDAR pattern (Cartesian co-ordinates).

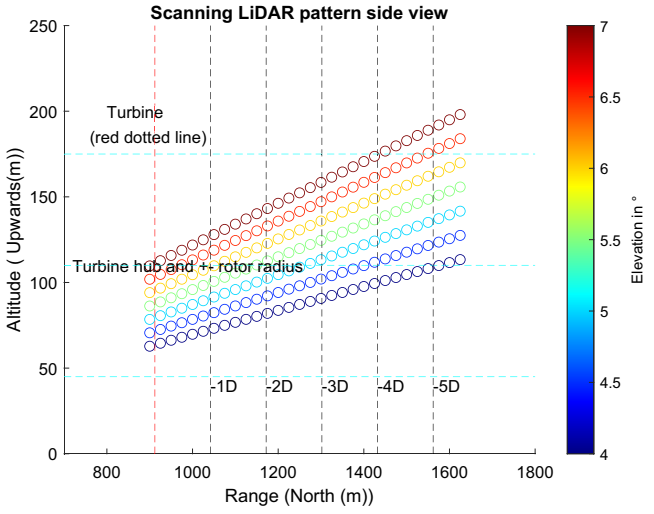

FIGURE A3 | Scanning LiDAR pattern side view.

Appendix B

Wind Component Retrieval

For the nonlinear squares method, Equation (1) (radial velocity expressed in relation to the u, v, w components of the wind velocity) was solved with $w = 0$, and the Levenburg-Marquardt algorithm was used to fit the u and v components, given the radial wind speed (V_r) and the scanning LiDAR azimuth (ψ) and elevation (θ) in a nonlinear least squares sense. The Maximum A Posteriori (MAP) method is a Bayesian estimation that incorporates prior beliefs about the unknowns, and then the posterior distribution of the unknowns is updated. This method is equivalent to the commonly used maximum likelihood estimation (MLE) when the said priors are uniform, that is, equal distribution of probabilities. For implementing MAP, Weibull priors were specified for u, v components in the wind sectors of 190° to 250° sector by ground-based profiling LiDAR measurements at hub height. The results indicate unrealistic estimates from the nonlinear least square fitting method, especially on the edges of the scan, see also Figure B1. The MAP method did not suffer from this issue but was computationally expensive. Based on the results of the comparison, the above-mentioned wind direction assumption approach is used for the results presented in this study for its computational ease and applicability in the wake sectors analyzed in this study. Furthermore, the results of the different methods at a 50 % span location (Figure B2) revealed a similar trend with slightly different magnitudes.

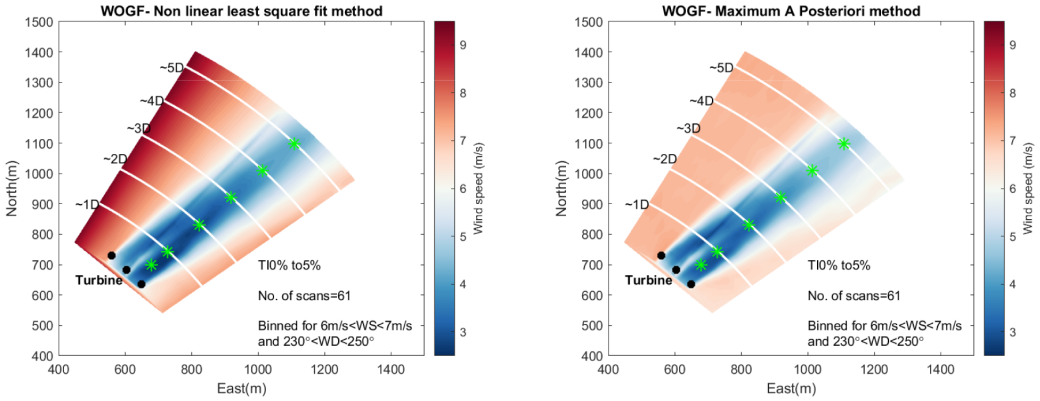

(a) Non linear least square fitting comparison

(b) Maximum A Posteriori estimation comparison

FIGURE B1 | Horizontal wind speed $\left(\sqrt{u^2+v^2}\right)$ example for a bin of $(6m/s < U_{\infty,hub} < 7m/s)$ (green asterisks: 50% span location).

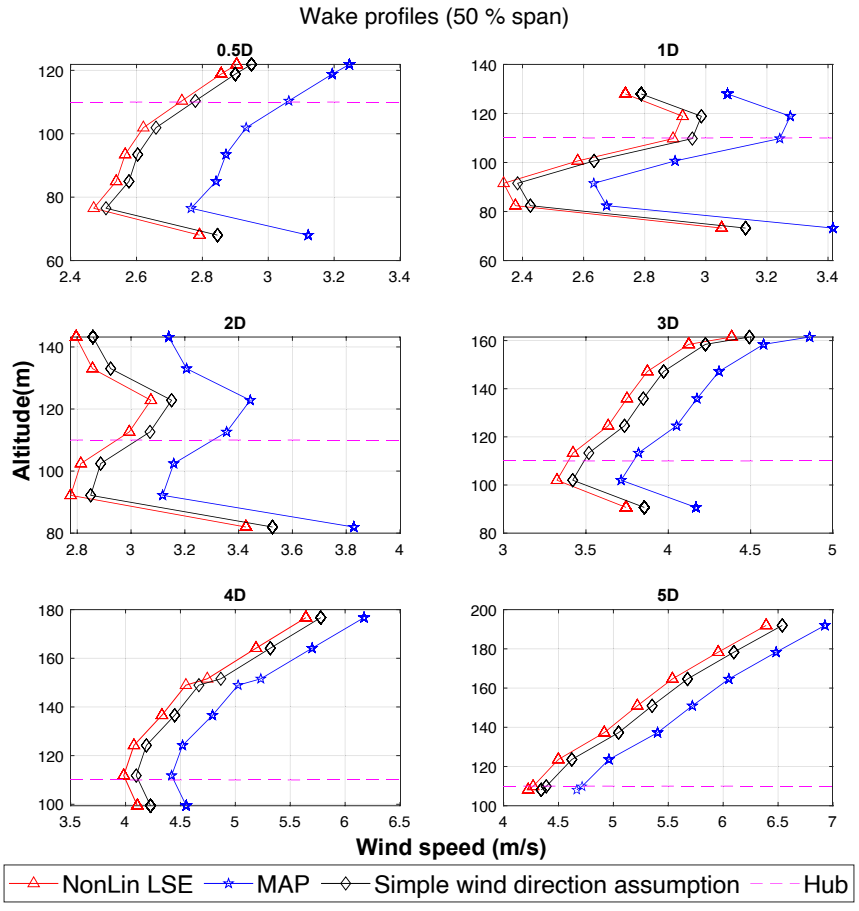

FIGURE B2 | Vertical profile comparison of different methods of wind component retrieval (6 m/s < $U_{\infty,hub}$ < 7 m/s).